



PCCP

**Inferring Relative Dose-dependent Color Center Populations
in Proton Irradiated Thoria Single Crystals using Optical
Spectroscopy**

Journal:	<i>Physical Chemistry Chemical Physics</i>
Manuscript ID	CP-ART-11-2021-005191.R1
Article Type:	Paper
Date Submitted by the Author:	05-Feb-2022
Complete List of Authors:	Khanolkar, Amey; Idaho National Laboratory, Materials Science and Engineering Dennett, Cody; Idaho National Laboratory, Materials Science and Engineering Department Hua, Zilong; Idaho National Laboratory, Materials Science and Engineering Department Mann, James; Air Force Research Laboratory, Sensors Directorate Hurley, David; Idaho National Laboratory, Materials Science and Engineering Department Khafizov, Marat; The Ohio State University, Mechanical and Aerospace Engineering

SCHOLARONE™
Manuscripts

ARTICLE

Inferring Relative Dose-dependent Color Center Populations in Proton Irradiated Thoria Single Crystals using Optical Spectroscopy

Received 12th November 2021,
Accepted 00th January 20xx

Amey Khanolkar,^{*a} Cody A. Dennett,^a Zilong Hua,^a J. Matthew Mann,^b David H. Hurley,^a and Marat Khafizov^{c†}

DOI: 10.1039/x0xx00000x

We have utilized photoluminescence spectroscopy and optical ellipsometry to characterize the dose-dependence of the photoluminescence emission intensity and changes in optical absorption of thoria single crystals subject to irradiation with energetic protons at room- and elevated-temperatures. The photoluminescence peaks and the optical absorption bands are attributed to creation of new electronic states emerging from defects resulting from displacement damage. These bands are most likely associated with electrons trapped at the oxygen vacancy sites similar to color centers formed in other irradiated oxides and halides. Our experimental observations are supported by a standard density functional theory calculation of the electronic structure in pristine and oxygen vacancy-bearing thoria crystals. The dose-dependence of the intensity of the photoluminescence peaks is used to parameterize a rate theory model that estimates the concentration of color centers in the irradiated crystals. This parameterization provides optimized migration barrier parameters for oxygen interstitials and vacancies that simultaneously capture the optical response of the crystals irradiated at room- and elevated-temperature. These optical spectroscopy techniques offer a promising pathway to characterize the population of color centers formed at the sites of oxygen anion vacancies, particularly in irradiated nuclear fuels, where atomic-level defects cannot be readily imaged using electron microscopy. When combined with other direct and indirect characterization tools, our approach can provide new insight into defect formation and accumulation in energy materials over single atomic to extended length scales.

Introduction

Metal oxides are a class of crystalline materials that exhibit unique properties, such as high mechanical strength, optical transparency, exceptional carrier mobilities and high abundance, all of which make these materials attractive for use in a variety of technological applications.¹⁻⁴ Actinide and lanthanide oxides in particular have garnered considerable attention owing to their technological relevance in energy materials, ranging from use as nuclear fuels in commercial and next generation reactors,⁵ catalysts for chemical reactions,⁶ and electrolytes in solid oxide fuel cells.⁷ The performance of these metal oxides in energy applications, that includes thermal and mass transport properties, is governed by their microstructure.² Under coupled extremes of temperature, energetic particles

bombardment, mechanical stress, or corrosive environments, the microstructure of these materials can rapidly evolve and lead to the formation of atomic level as well as extended structural defects.⁸ These defects introduce distortions in the crystal lattice that act as scattering sites for phonons and can drastically alter thermal⁹⁻¹¹ and elastic¹² properties. Furthermore, the optical properties of metal oxides may also be dramatically affected by the presence of point defects.¹³⁻¹⁵ Although ultrahigh resolution electron microscopy has been extensively employed to quantify the size, orientation, and density of extended lattice defects such as dislocation loops,¹⁶⁻²⁰ particularly in irradiated oxide nuclear fuels, obtaining statistically significant populations of atomic-level defects in such materials is challenging using microscopy-based direct imaging approaches.²¹ This has necessitated the application of indirect techniques to characterize lattice point defects.

In metal oxides, point defects in the oxygen sublattice can comprise of a neutral interstitial O_i and vacancy V_O , or a vacancy with one or two trapped electrons (referred to as F^+ and F centers, respectively, or color centers in general), along with their complementary charged O_i^- and O_i^{2-} interstitial defects.¹⁴ Cation vacancies can trap holes and transform into V^- or V^0 centers (cation vacancies with one or two holes, respectively).^{14, 22} Changes in the optical properties of metal oxides are attributed to, in part, the electronic transitions between defect levels created by the localization of electrons in F-center type

^a Materials Science and Engineering Department, Idaho National Laboratory, 1955 N. Fremont Ave., Idaho Falls, ID 83415 USA.

^b Air Force Research Laboratory, Sensors Directorate, 2241 Avionics Circle, Wright Patterson AFB, OH 45433, USA.

^c Department of Mechanical and Aerospace Engineering, The Ohio State University, 201 W 19th Ave, Columbus, OH 43210, USA.

* Email: Amey.Khanolkar@inl.gov

† Email: khafizov.1@osu.edu

Electronic Supplementary Information (ESI) available: [details of any supplementary information available should be included here]. See DOI: 10.1039/x0xx00000x

defects.^{14, 15} In the classical theories for optical absorption due to defects developed by Smakula²³ and by Mollwo and Roos,²⁴ electrons are described as a collection of independent Lorentz oscillators each with a frequency-dependent polarizability. The oscillator strength for a transition associated with a defect is related to the area under its absorption band that is assumed to be Lorentzian.¹⁵ Optical absorption (OA) and photoluminescence (PL) spectroscopy have been widely used to probe the absorption bands and energy levels of electrons associated with anion vacancies.^{25, 26} Experimentally measured optical absorption and photoluminescence energies of single vacancy centers in metal oxides such as MgO, CaO, SrO, BaO, and Al₂O₃ have been reviewed in reference.¹⁴ A combination of high temperature annealing, electron spin resonance (ESR) spectroscopy, and optical techniques have been used to isolate individual contributions to absorption and luminescence from F⁺ and F centers.²⁷⁻²⁹

Other indirect characterization techniques, such as positron annihilation spectroscopy (PAS),³⁰ most effective at probing vacancy-type defects,³¹⁻³⁵ and Rutherford backscattering spectroscopy (RBS),³⁶ more sensitive to interstitial-type defects,^{37, 38} have also been applied for analysis of defects in metal oxides. Of the lanthanide and actinide oxides, optical characterization studies of anion vacancies include works on ceria (CeO₂)^{39, 40} and urania (UO₂).⁴¹ Despite the technological relevance of thoria (ThO₂), there have been very limited recent experimental studies that have drawn connections between changes in radiation-induced optical properties and populations of vacancy point defects. This has been primarily due to the difficulty in growing high-quality single crystals of thoria stemming from its extremely high melting temperature.⁴²

Early studies that investigated changes in the optical absorption spectrum of crystalline thoria induced by heating the samples in air and in vacuum at temperatures up to 1800°C were published in the 1950s.^{43, 44} The presence of F-centers in single crystal thoria subject to ionizing radiation was first reported by Neeley and co-workers using ESR spectroscopy in 1967.⁴⁵ Subsequent studies on single crystal thoria in the 1970s investigated the effects of irradiation and annealing conditions on the optical absorption,^{46, 47} photoluminescence⁴⁸ and thermoluminescence^{49, 50} behavior of thoria. Regions of the sample exposed to ion irradiation changed color to an intense blue due to the formation of distinct optical absorption peaks. These optical absorption bands were attributed to the presence of electron or hole centers. Photoluminescence of arc fused ThO₂ single crystals following excitation with UV light exhibited sharp line spectra, characteristic of accidentally incorporated rare earth impurities and broad band spectra of the host lattice following annealing at high temperature.⁴⁸ The intensity of the broad asymmetric emission band at 2.76 eV (450 nm) was enhanced by annealing in a reducing environment due to the expected increase the oxygen vacancy concentration. It was suggested that the broad asymmetric emission band at 2.76 eV in the visible may be attributed to closely overlapping F and F⁺ centers stemming from oxygen vacancies in the lattice. A comparison of the optical absorption of flux-grown and arc-fused thoria single crystals under different annealing

conditions, and under gamma and UV radiation was presented by Griffiths and Dixon in 1992.⁵¹ Recently, Mohun and co-workers reported in situ photoluminescence of sintered polycrystalline thoria pellets during alpha irradiation, where the appearance of PL peaks in the visible spectrum during irradiation was attributed to the formation of electronic defect states.⁵²

While previous optical spectroscopy studies on thoria provided insight into the possible origins of optical absorption and photoluminescence bands, a systematic investigation involving the correlation between the magnitude of optical absorption and PL peaks and lattice point defect population in thoria has not been previously reported. Here, we perform steady-state room temperature PL and optical absorption spectroscopy on thoria single crystals following irradiation with 2 MeV protons (H⁺ ions) at room temperature and at 600°C to surface-confined damage levels in displacements per atom (dpa) ranging from 0.016 dpa to 0.79 dpa. Energetic protons have been shown previously to produce color centers in the thoria single crystals⁴⁶. The PL spectra reveal a broad asymmetric peak at ~1.67 eV and another lower intensity peak at ~1.92 eV. Distinct optical absorption peaks are seen at ~1.8 eV and ~2.0 eV in the optical absorption spectra of the irradiated thoria crystals. Due to the lack of previous electronic structure calculation using density functional theory (DFT) that resolves the excited state of oxygen vacancies, we performed simplified analysis to estimate the latter. Our results suggest that these peaks can be attributed to the presence of neutral and positively charged oxygen vacancies in the lattice. The relative change in the intensity of the PL and optical absorption peaks with displacement damage dose in combination with previously reported extended defect characterization is used to parameterize a rate theory model that estimates the concentration of oxygen anion vacancies in the irradiated thoria crystals. When coupled with other experimental techniques such as electron spin resonance spectroscopy, PAS, Raman scattering and X-ray diffraction (XRD), the optical spectroscopy-based approach will provide new insight into early-stage nanoscale defect evolution in metal oxide materials that cannot be readily resolved through electron microscopy.

Materials and Methods

Single crystals of thoria were grown using the hydrothermal synthesis method,^{42, 53} with feedstock of thoria powder and a cesium fluoride mineralized solution placed in an inert silver ampoule. The feedstock and crystallization zones were separated using a silver baffle in the ampoule and were maintained at 750°C and 690°C, respectively, using band heaters placed on the exterior walls of the autoclave in which the assembly was placed. These conditions were maintained for 10 days to facilitate crystal growth, before allowing the reaction to return to room temperature. Details of the crystal growth process are provided in reference.¹⁷ The crystals were mounted on copper blocks using silver paste with the {001} facet parallel to the face of the copper mount prior to ion beam irradiation.

Table 1. Summary of thoria single crystal samples along with the irradiation conditions. Samples have been assigned an ID for reference in the main text.

Sample ID	Ion Fluence (ions/cm ²)	Average Plateau Dose (dpa)	Average Dose Rate in Plateau Region (dpa/s)	Irradiation Temperature
Pristine	-	-	-	-
RT01	1.73×10^{17}	0.016	1.66×10^{-6}	Room temperature
RT02	8.64×10^{17}	0.079	1.66×10^{-6}	Room temperature
HT01	1.73×10^{18}	0.16	1.66×10^{-6}	600°C
HT02	5.18×10^{18}	0.47	1.66×10^{-6}	600°C
HT03	8.64×10^{18}	0.79	1.66×10^{-6}	600°C

Five mounted thoria crystals were exposed to 2 MeV protons (H⁺ ions) at both room temperature (two samples) and 600°C (three samples) using the 3 MV Tandem Pelletron accelerator at Texas A&M University.¹⁷ The facets of the ThO₂ crystals were exposed to the proton beam that was raster scanned with a 20% overlap to ensure a uniform dose across the sample surface. The ion flux was maintained at 1.8×10^{13} ions/cm²s. The irradiations were performed to target ion fluence levels in the range of 1.73×10^{17} ions/cm² – 8.64×10^{17} ions/cm² for room temperature irradiations and 1.73×10^{18} ions/cm² – 8.64×10^{18} ions/cm² for the 600°C irradiations.⁵⁴ Microstructural point defects are sufficiently mobile at 600°C and have been shown to recombine or cluster into extended defects in the crystals irradiated at 600°C¹⁷. The displacement damage profile in the depth created by the energetic protons was calculated using the Stopping Range of Ions in Matter (SRIM) code in the full cascade mode.^{55, 56} The SRIM calculations revealed a “plateau” damage region consisting of an 18 μm surface layer, followed by peak displacement damage occurring at 24 μm in the depth from the surface. This damage depth is well-suited for optical spectroscopy measurements within the “plateau” damage region. Details of the SRIM calculations and the experimental parameters used in the ion irradiations are provided in reference.¹⁷ Table 1 summarizes the average dose in displacements per atom as well as the average dose rate in the “plateau” region for the samples investigated in this work.

Steady-state PL measurements were performed on a pristine (unirradiated) and the irradiated thoria crystals at room temperature. A 532 nm continuous wave (CW) laser beam emitted by a Coherent Verdi laser was used for photoexcitation and was focused with normal incidence on the {001} face of the crystal to a ~2 μm diameter spot using a 50x objective lens in a Horiba LabRAM HR confocal microscope. Although the photoexcitation energy (2.33 eV) is below the bandgap of thoria, the PL measurements provide the ability to probe newly-created electronic levels in the defect-bearing thoria crystals with energies in the lower end of the visible segment of the electromagnetic spectrum. The power of the laser beam incident on the sample was ~450 μW. The laser beam passed through a confocal pinhole of diameter 400 μm, and a motorized slit set to a width of 100 μm. Photons emitted by the sample following photoexcitation were detected using a long focal length (800 mm) Czerny-Turner type spectrograph in the spectral range of 2.25 eV to 1.31 eV (950 nm to 550 nm) with a grating of 600 lines/mm mounted on a software-driven motorized turret. A multichannel air-cooled CCD detector with

1024 x 256 pixels and a pixel size of 26 μm x 26 μm was used for detection. PL spectra were acquired with an exposure time of 20 s and averaged over 2 accumulations. The spectra were acquired over multiple regions of the sample to ensure repeatability and that representative spectra were used for further analysis. The {001} facets of the thoria crystals being parallel to the copper mount ensured normal incidence of the photoexcitation laser beam in the photoluminescence experiments and enabled direct comparison of the PL intensities from spectra measured on different samples.

Due to the irregular shape of the crystals, we perform spectroscopy ellipsometry measurements in lieu of optical absorption spectroscopy in transmission mode. The real and imaginary parts of the complex optical reflectance of the pristine and irradiated thoria crystals were measured using a rotating compensator variable angle spectroscopic ellipsometer (M-2000V, J.A. Woollam Company). This technique has been used previously to evaluate vacancy defects-induced changes in optical properties of nickel oxide, a wide band gap semiconductor.⁵⁷ As opposed to transmission mode optical absorption spectroscopy that is predominantly sensitive to optical properties through the bulk of the sample, spectroscopic ellipsometry in glancing incidence reflection mode offers high sensitivity to surface-confined properties.⁵⁸ This technique is therefore well-suited for measuring changes in micrometer-thick surface damage layers created by ion irradiation. Spectroscopic ellipsometry data were acquired at angles of incidence ranging from 45° to 75°, in increments of 5°, by focusing polarized white light (derived from a 50 W quartz tungsten halogen lamp) to a ~300 μm spot on the sample. Changes in the s- and p-polarization state of white light after reflection off the sample surface were measured by directing the reflected light to a receiver unit that houses a polarizer mounted on a motorized rotational stage, and were characterized by the ellipsometry parameters Ψ and Δ that are related to the ratio of the reflectivity ρ for p- and s-polarized light as follows:

$$\tan(\Psi) \cdot e^{i\Delta} = \rho = \frac{r_p}{r_s} \quad (1)$$

where r_p and r_s denote the reflectivity of the sample to p- and s-polarized light, respectively. The $\tan(\Psi)$ and Δ terms in Eq. (1) represent the magnitude and phase, respectively, of the complex reflectivity ratio ρ. A fiber optic cable (with a 200 μm core diameter) was used to couple the light beam from the receiver unit to a detector with a UV spectrometer in the range

of 1.24 eV to 3.54 eV (1000 nm to 350 nm). The spectral dependence of the real and imaginary parts of the refractive index and the complex dielectric function were obtained by fitting the raw reflectance data to a 'General Oscillator' model described in the next section.

DFT was used to calculate the electronic band structure of the thoria lattice bearing neutral and positively charged oxygen vacancies, following the methodology in references.⁵⁹⁻⁶¹ The calculation is based on the local density approximation (LDA). A $2 \times 2 \times 2$ primitive cell was used as the basis for the DFT calculations using Perdew-Zunger LDA⁶² implemented within the Quantum ESPRESSO (QE) software.⁶³ Calculations were performed on $4 \times 4 \times 4$ k grid using an energy cut off of 950 eV and a convergence threshold of 1.0×10^{-7} eV. This resulted in a lattice parameter $a = 5.512 \text{ \AA}$, which is $\sim 1.5\%$ lower than the lattice parameter $a_{exp} = 5.597 \text{ \AA}$ measured on polycrystalline thoria using synchrotron X-ray diffraction.⁶⁴ The impact of oxygen vacancies on the electronic band structure was considered by removing one oxygen atom from the primitive cell, resulting in Th_8O_{15} stoichiometry. For neutral vacancy calculation the charge of the simulation cell was set to zero, whereas for the charged defects the charge of the cell was adjusted accordingly. Prior to band structure calculation, the structure was relaxed keeping the dimensions of the cell constant. The small number of atoms within the simulation cell allowed manual electron orbital assignment of each band within the vicinity of the electronic band gap based on symmetry analysis provide in QE.

The results of optical characterization were compared to a microstructure evolution model based on rate theory (RT) that tracks the concentration of oxygen vacancies as a function of displacement damage dose and irradiation temperature.^{65, 66} We implement a RT model that has been previously applied to study microstructure evolution under irradiation in ceria,⁶⁷ urania⁶⁸ and more recently, in same set of proton-irradiated thoria single crystals used in this study.⁵⁴ This model considers point defect evolution on cation and anion sublattices and includes interstitial-vacancy pair generation, their mutual recombination, and interstitial dislocation loop nucleation and growth.⁶⁸ No voids growth were observed from electron microscopy in these samples and therefore this process isn't considered in the RT model.⁵⁴ It should also be noted that in its current form, this RT model doesn't distinguish between neutral and charged defects. The rate theory model applicable to thoria has been previously parametrized based on the measurements of loop density and size from transmission electron microscopy (TEM) images in the 600°C irradiated crystals.⁵⁴

Results

Figure 1(a) and (b) show a top-down view of sample RT01, before and after irradiation with 2 MeV protons at room temperature to the lowest displacement damage dose of 0.016 dpa, respectively. The transparent pristine thoria crystals developed a deep blue color in the region exposed to the proton beam. This is consistent with a previously reported observation of color change following proton irradiation in commercial arc-

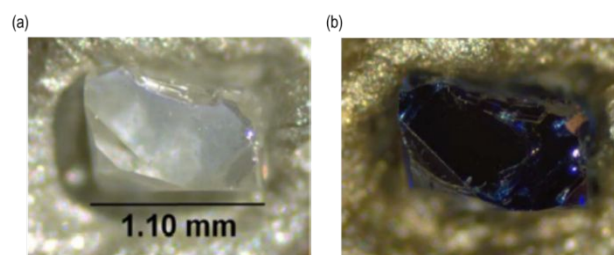


Figure 1. Optical micrographs showing (a) colorless and transparent pristine thoria single crystal before irradiation and (b) deep blue color in the same crystal following proton irradiation at room temperature to a damage dose of 0.016 dpa. The silver paste used to attach the crystals to a copper mount contributes to the shiny background around the crystals.

fused thoria single crystals.⁴⁶ The deep blue color in the irradiated crystals indicates the formation of color centers associated with point defects, where trapped electrons and holes contribute to emergence of new states in the electronic band structure.

The steady-state PL spectra measured following photoexcitation of the pristine and irradiated thoria crystals are shown in Fig. 2. The PL spectrum measured on the pristine sample show several narrow low-intensity peaks between 1.38 eV to 1.46 eV (shown in the inset of Fig. 2(a)), along with a higher intensity narrow peak at ~ 2.1 eV. These sharp line features were observed in the spectra recorded from multiple locations of the pristine crystal and may be attributed to luminescence from impurities.⁴⁸ Additionally, a background signal characterized by a gradual increase in the intensity of the PL spectrum with increasing photon energy is observed in the measurement on the pristine crystal. The PL spectra of the irradiated thoria crystals, on the other hand, show two distinct peaks – a dominant, asymmetric peak at ~ 1.67 eV, and another lower intensity peak at ~ 1.92 eV. The intensity of these PL peaks in the irradiated samples increases with increasing displacement damage dose and appears to saturate at high dose levels. To quantify the dose-dependence of the characteristics of the PL peaks, the PL spectra were fitted with multiple Gaussian peaks whose center energy E_i , amplitude A_i and width B_i were used as fitting parameters. An additional linear term was used to fit the gradual increase (background) in the spectrum intensity with increasing photon energy. For samples HT02, and HT03, two Gaussian terms were needed to fit the dominant asymmetric peak at ~ 1.67 eV. We note that narrow peaks in the range of ~ 2.1 eV – 2.25 eV, close to the excitation laser line, were also observed in the irradiated crystals. These peaks originate from Raman scattering of incident photons with defect clusters and have been discussed previously¹⁷. As such, only the peaks at ~ 1.67 eV and at ~ 1.97 eV were analyzed further.

The Gaussian peak decomposition of the measured PL spectra are shown in Fig. 2. The lower intensity peak at ~ 1.92 eV was fitted with a single Gaussian term with amplitude A_1 , center energy E_1 and width B_1 (shown with the red dotted curve) in all samples. The dominant peak at ~ 1.67 eV in the PL spectra was fitted with a single Gaussian with amplitude A_2 , center energy

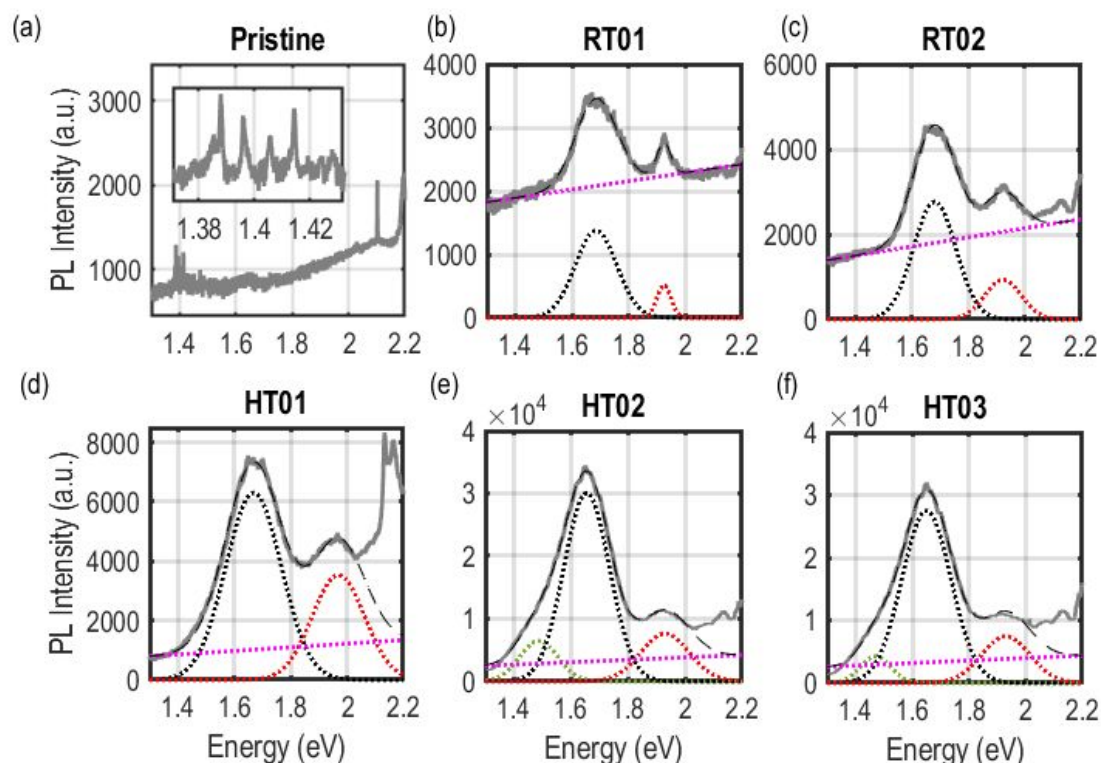


Figure 2. Raw PL spectra measured on the pristine and proton irradiated thoria single crystals, shown with the gray curves. For the irradiated crystals, the dashed black curve represents the sum of Gaussian terms fitted to the measured PL spectrum. An additional linear term (shown in magenta) was added to account for the background. The dominant peak at ~ 1.67 eV in the PL spectra measured in samples HT02 and HT03 was fitted with two Gaussian terms (shown with the dotted green and black curves).

E_2 and width B_2 (shown with the black dotted line in Fig. 2) except in the case of samples HT02 and HT03, where an additional Gaussian term (with amplitude A_3 , center energy E_3 and width B_3) was required to obtain an optimal fit of this peak (highlighted with the black and green dotted curves, respectively, in Fig. 2 (e) – (f)). The magenta dotted lines represent the linear background term fitted to the spectra. The sum of all fitted terms is represented by the black dashed curve in Fig. 2 and is plotted over the raw measured PL spectrum. Table 2 summarizes the values of the amplitude and center energy of the Gaussian terms fitted to the measured PL spectra.

From Table 2, we see that the amplitude of the Gaussian terms fitted at ~ 1.67 eV and at ~ 1.94 eV increases with displacement damage dose and shows a saturation at high dose. The center of the dominant Gaussian term at that was used to fit the asymmetric peak at ~ 1.67 eV also shows a general trend – the energy (E_2) of the Gaussian term shows a redshift with increasing damage dose. The center of the highest energy peak (E_1), on the other hand, varies between 1.92 eV to 1.97 eV, and does not exhibit any trend with damage dose. The third peak at ~ 1.48 eV fitted to the spectra of samples HT02 and HT03 was

Table 2. Summary of the amplitude, center energy and width of Gaussian peaks fitted to the measured PL spectra.

Sample ID	Average Plateau Dose (dpa)	A_1 (a.u.)	E_1 (eV)	B_1 (eV)	A_2 (a.u.)	E_2 (eV)	B_2 (eV)	A_3 (a.u.)	E_3 (eV)	B_3 (eV)
Pristine	-	-	-	-	-	-	-	-	-	-
RT01	0.016	521 ± 9	1.92 ± 0.001	0.04 ± 0.001	1377 ± 5	1.69 ± 0.0003	0.10 ± 0.0005	-	-	-
RT02	0.079	933 ± 7	1.92 ± 0.001	0.09 ± 0.001	2776 ± 6	1.68 ± 0.0002	0.11 ± 0.0003	-	-	-
HT01	0.16	3534 ± 59	1.97 ± 0.001	0.13 ± 0.001	6308 ± 30	1.67 ± 0.0002	0.14 ± 0.0005	-	-	-
HT02	0.47	7629 ± 80	1.93 ± 0.01	0.12 ± 0.01	30089 ± 61	1.66 ± 0.0004	0.11 ± 0.0004	6483 ± 106	1.49 ± 0.002	0.09 ± 0.002
HT03	0.79	7464 ± 88	1.93 ± 0.01	0.12 ± 0.01	27494 ± 66	1.65 ± 0.0003	0.12 ± 0.0004	4259 ± 84	1.47 ± 0.001	0.08 ± 0.002

used to capture the asymmetry in the dominant peak at ~ 1.67 eV and was not analyzed further.

In addition to PL, spectroscopic ellipsometry was used to elucidate irradiation-induced changes in optical properties by measuring the spectral dependence of the complex dielectric function and the real and imaginary parts of the refractive index of the pristine and irradiated thoria crystals. Figure 3 shows the raw Ψ and Δ parameters measured on the six samples at angles of incidence of 55° , 60° and 65° . In the case of the ellipsometry data obtained from the high temperature-irradiated samples, shown in Fig. 3(d) – (f), we observe distinct features at ~ 1.8 eV and ~ 2.0 eV. These features indicate the emergence of new peaks associated with radiation-induced lattice defects. A zoomed-in view of these features observed in the raw Δ data acquired at 65° angle of incidence on samples HT01, HT02 and HT03 is shown in the insets of Fig. 3(d) – (f), respectively.

To characterize the impact of radiation induced defect on the dielectric constants, we analyze the raw ellipsometry data by fitting the measured spectral dependence of the Ψ and Δ values to a ‘General oscillator’ model that utilizes Lorentz oscillators with center energy E_o , amplitude A_o , and width B_o to capture electronic transitions. The complex dielectric function is modeled using Lorentzian oscillators defined by the relation:⁶⁹

$$\epsilon = \epsilon_1 + i\epsilon_2 = \epsilon_\infty + \frac{A_o B_o E_o}{E_o^2 - E^2 - iEB_o} \quad (2)$$

Here, ϵ_∞ represents the static contribution to the real part of the dielectric function and was used as a fitting parameter in the model. The values of the Lorentzian oscillator center energy E_o , amplitude A_o , and width B_o were also kept as free

parameters while fitting the raw data to the model. In the case of the pristine sample, the general oscillator model comprised a single Lorentz oscillator whose center energy was fixed at 5.4 eV, corresponding to the band gap energy of thoria.⁷⁰ The width of this oscillator was fixed at 0.4 eV, in accordance with previously reported value.⁷⁰ This oscillator represents the fundamental valence-to-conduction band electronic transition (i.e., the O-2p to Th-6d or Th-7s transition). The amplitude of this Lorentz oscillator was left as a free parameter when fitting the raw data from the pristine sample to the General oscillator model. The substrate-ambient boundary condition was used in this case, in which the thoria single crystal is treated as an optically thick, quasi-infinite half-space.^{69, 70} The model also considered surface roughness as a fitting parameter. An ‘effective’ roughness layer is added to the model whose optical constants are derived by mixing the optical constants of the underlying material with those of a ‘void’ with $n = 1$, $k = 0$. The Bruggeman effective medium approximation is used to calculate the optical constants of the ‘composite’ surface roughness layer by assuming 50% void content. This effective medium approximation is valid when the size of the surface roughness is much less than the optical wavelength range in the measurement.⁶⁹ The raw Ψ and Δ data acquired at all angles of incidence were used for fitting to the ‘General oscillator’ model. An ‘angle offset’ term was also included in the model to specify an offset to the nominal angle of incidence in the experiment. The Ψ and Δ values obtained from the fit to the raw pristine sample data are plotted in Fig. 3(a) with the dashed black lines. Good agreement is seen with the experimentally measured Ψ and Δ values and this confirms the validity of using a single

Table 3. Summary of amplitude, center energy and width of Lorentzian peaks fitted to the measured complex reflectance data in spectroscopic ellipsometry.

Sample ID	ϵ_∞	Surface Rough (nm)	A_{o1} (a.u.)	E_{o1} (eV)	B_{o1} (eV)	A_{o2} (a.u.)	E_{o2} (eV)	B_{o2} (eV)	A_{o3} (a.u.)	E_{o3} (eV)	B_{o3} (eV)
Pristine	3.62 ± 0.008	4.54 ± 0.01	9.43 ± 0.07	5.4*	0.4*	-	-	-	-	-	-
RT01	3.49 ± 0.006	6.70 ± 0.01	11.76 ± 0.06	5.4*	0.4*	0.013 ± 0.002	1.75 ± 0.01	$0.3^* \pm 0.15$	0.012 ± 0.004	2.04 ± 0.02	$0.3^* \pm 0.15$
RT02	3.05 ± 0.004	6.49 ± 0.01	16.64 ± 0.05	5.4*	0.4*	0.020 ± 0.002	1.75 ± 0.01	$0.3^* \pm 0.15$	0.007 ± 0.002	2.00 ± 0.02	$0.3^* \pm 0.15$
HT01	3.60 ± 0.004	2.05 ± 0.01	10.35 ± 1.6	5.4*	0.4*	0.023 ± 0.002	1.80 ± 0.03	$0.1^* \pm 0.05$	0.018 ± 0.002	2.02 ± 0.01	$0.17^* \pm 0.05$
HT02	3.52 ± 0.008	1.09 ± 0.01	13.26 ± 0.08	5.4*	0.4*	0.025 ± 0.004	1.82 ± 0.01	$0.075^* \pm 0.1$	0.035 ± 0.008	2.03 ± 0.01	$0.12^* \pm 0.1$
HT03	3.68 ± 0.008	3.42 ± 0.01	11.02 ± 0.09	5.4*	0.4*	0.076 ± 0.002	1.77 ± 0.01	$0.3^* \pm 0.02$	0.060 ± 0.002	2.03 ± 0.01	$0.3^* \pm 0.02$

* fixed parameter

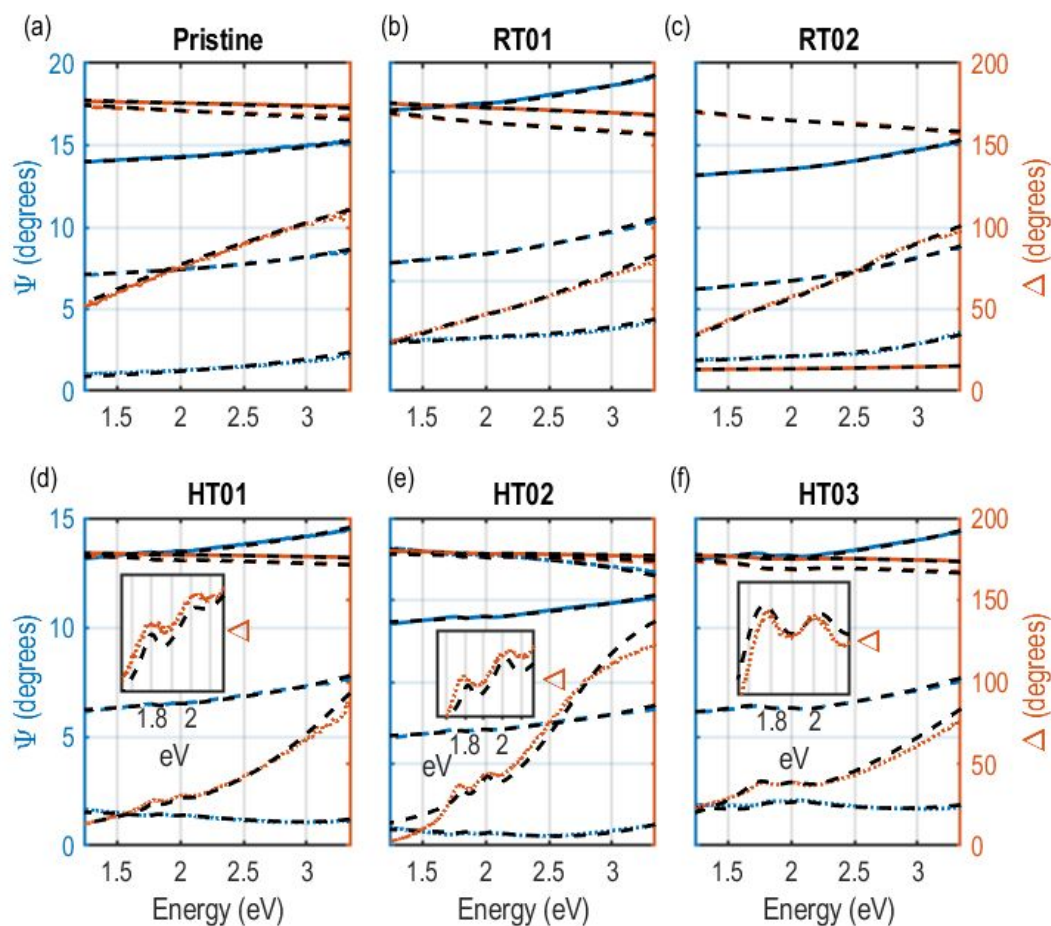


Figure 3. Raw ellipsometry Ψ and Δ values measured on the (a) pristine, (b) – (c) room temperature irradiated and (d) – (f) 600°C irradiated thoria samples at angles of incidence of 55°, 60°, and 65° in the spectral range of 1.24 eV to 3.5 eV. The dashed line denotes the corresponding values obtained from the General oscillator model fit to the raw data. The insets in panels (d) – (f) show zoomed-in views of the features in the raw values of Δ acquired at 65° angle of incidence in samples HT01, HT02, and HT03, respectively.

oscillator for modeling the valence-to-conduction band electronic transition in pristine thoria.

For the ellipsometry data measured on the irradiated thoria samples, the General oscillator model was modified to include two Lorentz oscillators in addition to the intrinsic Lorentz oscillator representing fundamental valence-to-conduction electronic transition. These additional Lorentz oscillators were used to capture changes in optical properties in the 1.7 - 2.2 eV range (Fig. 3) attributed to electronic transitions induced by lattice point defects within the damage layer. Like in the case of the pristine sample, the center energy and width of the intrinsic oscillator for the irradiated crystals were fixed at 5.4 eV and 0.4 eV, respectively, while the amplitude of this oscillator was left as a free parameter. The amplitude and center energy of the two additional oscillators that represented intermediate defect electronic states were kept as fitting parameters. Although distinct features were not discerned in the spectral dependence of the raw Ψ and Δ curves corresponding to the crystals irradiated at room temperature, the General oscillator model with two defect peaks was nevertheless used to fit these data. We hypothesize that the low concentration of lattice defects in the crystals irradiated at room temperature makes these peaks

indiscernible from the background. In this case, the fitting range of E_0 was limited to 1.75 – 1.85 eV for the first defect peak, and to 1.9 – 2.15 eV for the second defect peak. Our observation of PL peaks measured in the room temperature-irradiated crystals in the vicinity of these spectral locations further justified the inclusion of peaks for fitting in the spectra range of 1.75 – 1.85 eV and 1.9 – 2.15 eV. The width of the additional peaks in the data corresponding to the 600°C irradiated crystals was estimated from the Ψ and Δ curves and not used as fitting parameters in the model. The width of the defect peaks in the room temperature-irradiated crystals was fixed at the upper bound of 0.3 eV. In all cases, the value of ϵ_∞ , the surface roughness and the angle offset term were kept as free parameters for fitting. From Fig. 3, we see that the General oscillator model with two defect oscillators captures the peak-like features in the Ψ and Δ values measured on the irradiated samples. In the case of samples HT02 and HT03, shown in Fig. 3(e) – (f), although the fitted model reproduces the experimentally-measured Ψ values with reasonable accuracy, we see some deviation from the experimentally-measured Δ values in the spectral regions away from the peak-like features. Table 3 summarizes the parameters obtained by fitting the

General Oscillator model to the ellipsometry data. The fitted surface roughness parameter varied between 1-7 nm across all samples. The fitted values of ϵ_∞ were all within $\sim 2\%$ of each other. The fitted offset in the angle of incidence was less than 1° in all cases. Although accurately fitting the spectra dependence of Ψ and Δ is challenging, particularly for capturing sub-band gap absorption features associated with defect centers,⁷¹ we only use the model fit to estimate the amplitude of the defect peaks at ~ 1.8 eV and ~ 2.0 eV in the raw data.

Figure 4(a) and (b) illustrate the real (ϵ_1) and imaginary (ϵ_2) parts, respectively, of the complex dielectric function obtained from the fitting of the raw Ψ and Δ values to the General Oscillator model. From Fig. 4(a), we observe bipolar peaks at ~ 1.8 eV and ~ 2.0 eV in the spectral dependence of ϵ_1 for the irradiated samples. The spectral dependence of ϵ_2 in the irradiated samples shows peaks centered at ~ 1.8 eV and ~ 2.0 eV that are characteristic of optical absorption. We postulate that the intense blue coloration in the irradiated samples stems from these optical absorption peaks. The amplitude of the optical absorption peaks at ~ 1.8 eV and ~ 2.0 eV also increases with displacement damage dose.

Our DFT based calculations of the electronic band structure of pristine thoria are consistent with previous reports.⁷² Figure 5(a) shows a schematic representation of the band diagram which is characterized by the O-2p orbital in the valence band and closely overlapping Th-7s and Th-6d orbitals in the conduction band. The calculated electron band structure diagram is shown in the supplemental information.⁷³ The energy gap of 6.5 eV between the O-2p valence band to the overlapping Th-6d/7s conduction bands obtained from our DFT calculations is $\sim 22\%$ higher than the experimentally measured band gap of 5.4 eV,⁷⁰ while lower values of the band gap have been reported previously using DFT.⁷⁴ DFT calculations of the electronic structure of the defected supercell show the emergence of new bands (Fig. 5 (b-c)). One s-like band corresponding to the ground state of the F-center is located within the band gap. The location of this band is consistent with the previous DFT calculation in thoria that only reported the density of states.⁷⁴ A p-like band corresponding to an excited state of the F-center is resonant with the conduction band of pristine thoria. While the current result shows the formation of intermediate electronic levels in the band gap by neutral and charged oxygen vacancies on the order of the observed optical absorption energies,^{61, 75} more accurate first-principles calculations that consider the many-body and exciton effects could provide better agreement with experimental observations. However, this exercise is beyond the scope of this experimentally focused paper.

Discussion

We investigate the dose dependence of the PL and optical absorption intensities. A summary of the dose-dependence of the PL intensities and the dose-dependent optical absorption is presented in Fig. 6. Figure 6(a) shows the amplitude of the Gaussian peaks centered at ~ 1.67 eV and ~ 1.94 eV obtained by fitting measured PL spectra to broadened Gaussian terms. While the amplitude of each of the Gaussian terms increases with damage dose, we observe a saturation in the amplitude at high doses in the 600°C-irradiated samples. A similar trend of increasing amplitude with dose is seen in the amplitude of the Lorentz oscillators at 1.8 eV and 2.0 eV obtained by fitting the optical ellipsometry data, plotted in Fig. 6(b). A comparable dose-dependent trend involving a linear increase in optical absorption at low doses, followed by saturation at high dose, has been reported in alkali halides irradiated with swift heavy ions.^{76, 77} The PL intensity and the strength of the Lorentz optical oscillator are both proportional to the number of available electronic states that facilitate the transitions of electrons from lower to higher energy levels, and vice-versa.¹⁵ We parameterize the microstructure evolution model based on rate theory^{54, 66} using the dose-dependent PL peaks to estimate the concentration of oxygen vacancies that create F- and F⁺-centers at a given radiation dose level. The primary defect generation rates are calculated using SRIM by taking the applied ion beam dose rate as an input.⁵⁴ The model is parametrized by optimizing a conversion factor relating the intensities of the 1.67 eV and 1.94 eV PL peaks. The concentration of oxygen vacancies parametrized using the PL peak intensities in the rate theory model is shown in Fig. 6(c).

We note that the dose-dependent amplitudes of the Lorentz oscillators representing optical absorption bands were not used in the parameterization of the rate theory model due to the uncertainty in the amplitudes of the absorption peaks in the room temperature irradiated samples. Our rate theory model predicts a saturation of oxygen vacancies to a concentration of $\sim 4.5 \times 10^{-6}$ /atom at very low levels of radiation dose for proton irradiation at room temperature, while for the samples irradiated at 600°C, the radiation dose needed to reach saturation of oxygen vacancies is much higher. The model shows that the concentration of oxygen vacancies is $\sim 1.5 \times 10^{-4}$ /atom at the highest radiation dose of 0.79 dpa and continues to slowly rise with dose for proton irradiation at 600°C. A larger concentration of oxygen vacancies at higher temperatures appears counterintuitive if one considers only oxygen-interstitial recombination process for damage recovery. However, we recognize that the achieved dose of high temperature samples corresponds to a dislocation loops growth regime, where an alternative pathway for interstitials

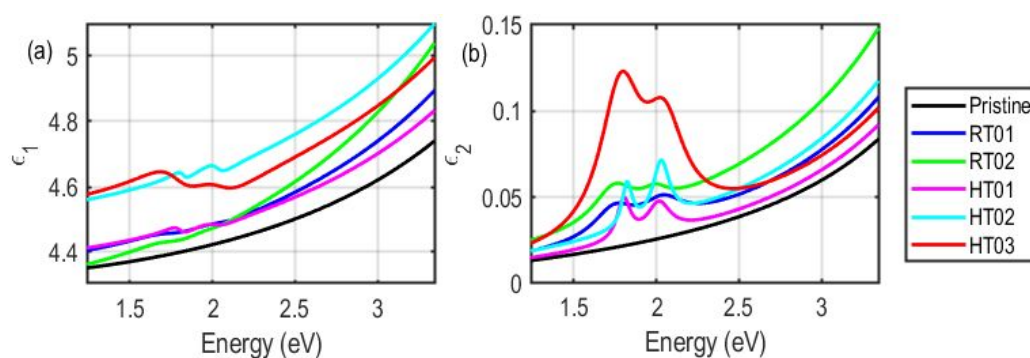


Figure 4. The spectral dependence of the (a) real (ϵ_1) and (b) imaginary (ϵ_2) parts of the complex dielectric function in pristine and irradiated thoria obtained from the 'General Oscillator' model fit to the measured ellipsometry data.

characterized by absorption of interstitials by dislocation loops, limits the recombination of Frenkel pairs, leaving behind a population of oxygen vacancies increasing until onset of void or vacancy cluster formation.^{54,65} Evaluating the dose dependence of the PL intensities at higher doses than considered here could provide further insight into the evolution and recombination of oxygen vacancies at elevated temperatures.

The Gaussian broadened PL peaks in the spectra measured in this work have similar characteristics to those reported previously in metal oxides with oxygen vacancy-type point defects such as thoria,⁴⁸ MgO,^{27, 28} and Al₂O₃.⁷⁸ It has been hypothesized that the broad and asymmetric PL bands may be due to closely overlapping F- and F⁺-centers.⁴⁸ Rinke and coworkers combined density functional theory with a many-body perturbation theory by including the electron-hole and electron-phonon interactions to calculate the optical absorption and luminescence spectra of the oxygen vacancy in MgO in all three charge states.⁷⁵ Their calculated optical absorption and luminescence bands agreed well with corresponding experimental data. Although our DFT calculations neglect many-body and exciton effects, we see that

lattice lead to the observed PL and optical absorption (OA) bands. We note that the energy of the PL bands is slightly lower than that of the absorption bands. This may be attributed to many-body effects where upon transition of the electron to the excited state, the system equilibrates to a lower energy configuration. When the excited electron relaxes, the transition to a ground state has a lower energy.^{59, 75}

In addition to DFT, the optical absorption energy E_{abs} due to color centers can be estimated using a modified version of the empirical Mollwo-Ivey relation, $E_{abs} = Cd^{-n}$,²⁴ that is based on the 'particle in a box' model. Here, $C = 17.3 \pm 1.7$ eV is a universal prefactor, d is the lattice parameter in Angstroms, and $n = 1.81 \pm 0.1$.^{79, 80} Using the experimentally determined lattice parameter of $a = 5.597$ Å,⁶⁴ we obtain $E_{abs} = 2.47$ eV. This value is marginally higher than the ~ 1.8 eV and ~ 2.0 eV optical absorption peaks measured using ellipsometry. Future studies utilizing DFT calculations of the electronic structure that include many-body and exciton effects could provide further insight into electronic band structure, and subsequent changes in PL and optical properties induced by F-, F⁺, or F²⁺-type anion vacancy centers and other defects.⁸¹ Based on the experimental

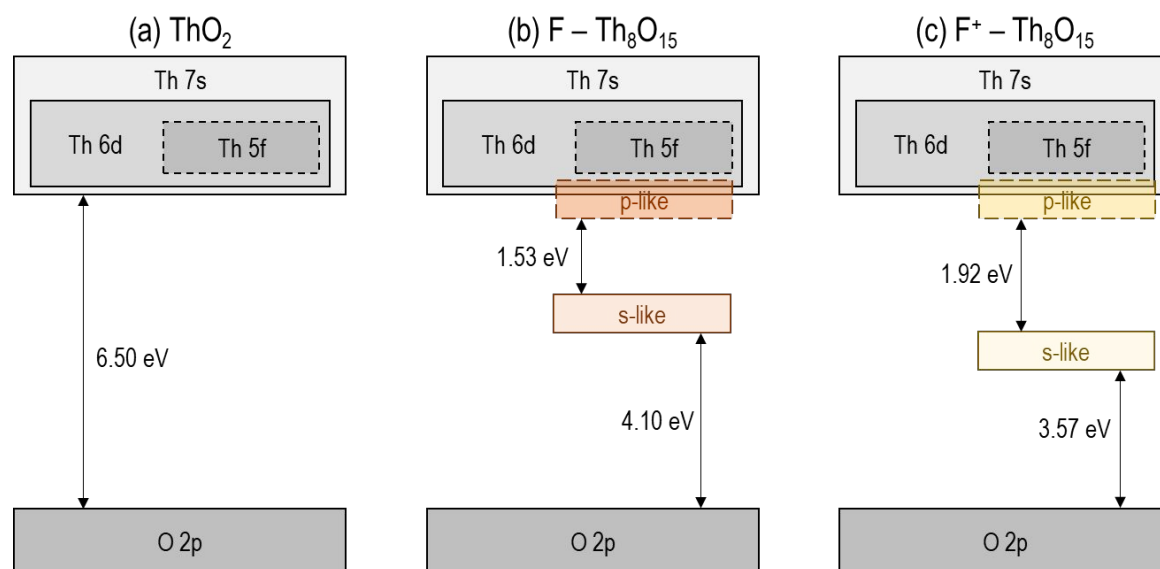


Figure 5. Electronic structure under independent particle approximation for (a) perfect crystal, (b) F-center, and (c) F⁺ center in thoria.

the separation between *s*- and *p*-like electronic levels created by the removal of an oxygen atom in the supercell are comparable to the photon energy associated with the observed PL and optical absorption peaks. The limitation of the simplified analysis conducted here has been recognized in the aforementioned reports in other oxides but serves as a reasonable initial step considering the lack of first-principles studies of color centers in thoria. Based on our preliminary analysis, we attribute the lower ~ 1.67 eV PL peak and the ~ 1.8 eV optical absorption peak to the presence of F-centers, while the higher ~ 1.94 eV PL peak and the ~ 2.0 eV optical absorption peak may be attributed to the generation of F⁺-centers under irradiation. We suggest that these new electronic levels that are created due to neutral or charged oxygen vacancy sites in the

observations and our DFT calculations, we present a schematic representation of the possible electronic transitions in the defect-bearing thoria crystals due to F- and F⁺-centers using a one-dimensional configuration coordinate diagram⁸² shown in Fig. 7. The potential curves shown in orange in Fig. 7 represent the intermediate electronic levels created by electrons trapped at the color center sites.

The results of the optical characterization can be put in perspective of microstructure evolution under irradiation

to those used in the RT model in reference⁵⁴ and listed in Table 4. It should also be noted that the thorium vacancies are

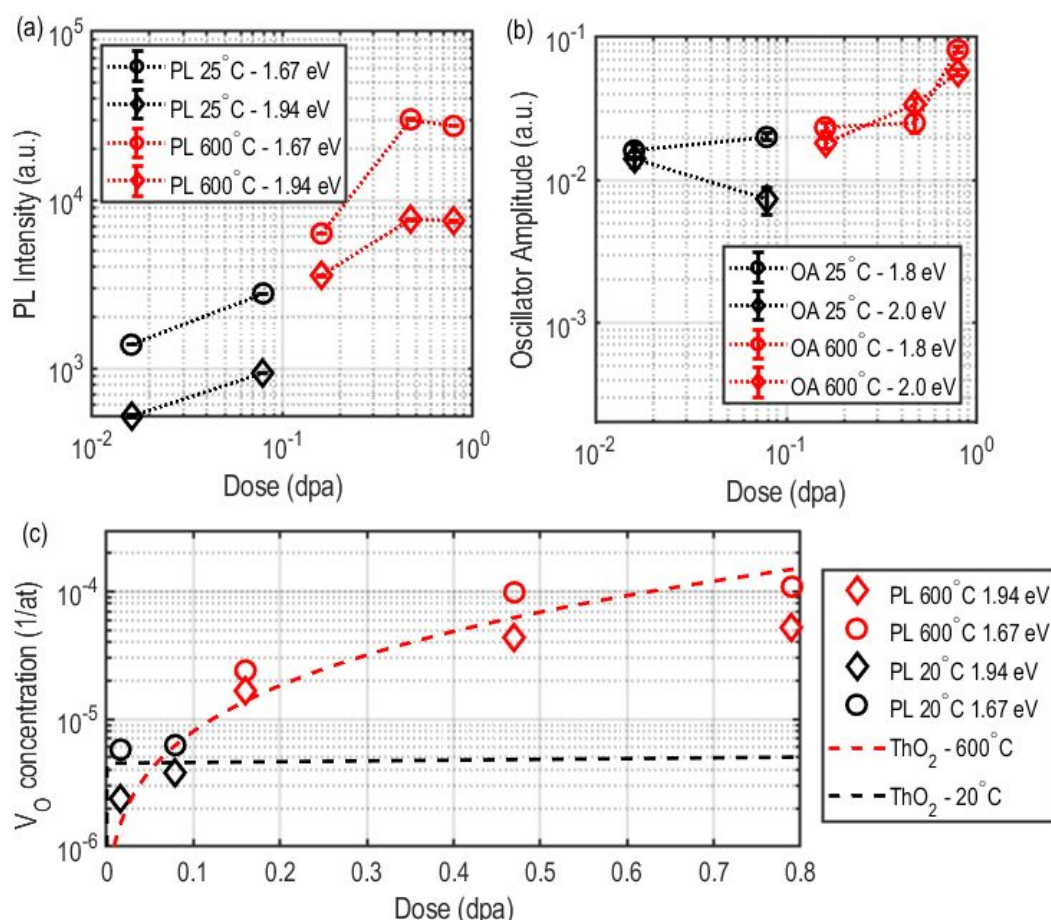


Figure 6. Dose dependence of the (a) PL intensities and (b) Lorentz oscillator amplitudes that represent optical absorption (OA) bands in the thoria crystals irradiated with energetic protons at room temperature and at 600°C. The concentration of oxygen vacancies with radiation dose is estimated from the PL peak intensities using rate theory and is shown in panels (c).

previously discussed in reference.⁵⁴ Even though the existing RT model applied to describe the behavior of this system lacks the additional details of neutral and charged vacancies, it allows us to gauge the utility of these results in understanding microstructure evolution in this system. For example, the migration barrier parameters optimized for the analysis of 600°C irradiated crystals in reference⁵⁴ are unable to adequately capture the optical response of both low- and high temperature-irradiated crystals simultaneously. However, after performing further parametrization of the model by refitting experimental data (including measurements of the size and density of dislocation loops imaged using TEM) from reference⁵⁴ with data from photoluminescence measurements in this work, we obtain a model that captures the optical response of both low- and high temperature-irradiated crystals (Fig. 6c). The new parametrization keeps the migration barrier for the thorium interstitial practically unchanged but provides more noticeable adjustments to migration barriers of oxygen defects. The adjusted values of the migration barriers obtained by parameterizing the PL measurements in this work are compared

immobile under the considered irradiation conditions.

The optical spectroscopy techniques utilized in this study, when combined with other characterization techniques, could provide a multimodal pathway to understanding defect formation, clustering, and recombination mechanisms. In

Table 4. Migration barriers (in eV) for thorium interstitials (Th_i), oxygen interstitials (O_i), and oxygen vacancies (V_O) for the RT model.

	Th _i	O _i	V _O
Dennett et al. ⁵⁴	2.86	0.72	1.49
Current work	2.83	0.56	1.76

addition to defect characterization, multimodal techniques can also be applied towards assessing the impact of microstructural defects on pertinent material properties. For instance, the degradation in the thermal conductivity of the same set of proton-irradiated thoria crystals was measured using a modulated spatial-domain thermoreflectance technique.^{17, 54} The large reduction in the thermal conductivity of thoria crystals irradiated at room temperature, compared to the lower reduction in the thermal conductivity of the thoria crystals

irradiated at 600°C was attributed to defect clustering and an overall reduction in phonon scattering for the 600°C-irradiated samples.¹⁷ Transmission electron microscopy (TEM) can be used to obtain the size and density of extended defects such as dislocation loops.⁸³ X-ray photoemission spectroscopy (XPS) has been previously used to determine the oxidation state of soluble impurities in thoria,⁸⁴ and could be used as a complimentary tool to optical spectroscopy by verifying changes in electron binding energies from lattice defects. Raman spectroscopy has been used to infer the defect structure and chemical composition from the vibrational modes of small-scale defect clusters in proton-irradiated actinide oxide crystals^{17, 37} and urania pellets with varying stoichiometry.⁸⁵ X-ray diffraction (XRD) has also been applied to infer radiation-induced volumetric changes to lattice, in combination with mesoscale thermal transport measurements and transmission electron microscopy in ion-irradiated urania^{86, 87} and ceria,⁶⁷ and other ceramic materials.⁸⁶ Combining the optical spectroscopy approach presented here, with other techniques such as modulated thermoreflectance, Raman spectroscopy, TEM and XRD offers the potential for a comprehensive characterization of the nature and population of point- and extended defects in irradiated metal oxides. Besides serving as a route to characterize early-stage radiation-induced defects in insulators, this multimodal approach may also be applied for quantifying the size and density of defects seeded in the microstructure in a controlled fashion with the objective of tailoring the refractive index of semiconductors and insulators for practical applications in microelectronic devices and sensors such as high-performance optical waveguides in lithium niobate,⁸⁸ or sapphire-based optical fiber claddings for harsh environment sensing.^{89, 90}

Conclusions

We have studied the dose-dependence of photoluminescence and optical absorption intensity in thoria single crystal irradiated with energetic protons to displacement damage levels ranging from 0.016 dpa to 0.16 dpa at room temperature and at 600°C. We observe a broad, asymmetric peak at ~ 1.67 eV, and another lower intensity peak at ~ 1.94 eV in the PL spectra. The optical absorption measurements show two distinct absorption bands at ~ 1.8 eV and ~ 2.0 eV in the crystals irradiated at 600°C. The PL and optical absorption intensities increase with radiation dose, and approach a saturation limit in the high temperature, high dose regime. Using simple density functional theory calculations of the electronic band structure, we attribute the observed PL and optical absorption to intermediate electronic transitions associated with electrons trapped in neutral and charged oxygen anion vacancies in the lattice, known as F- and F⁺-centers, respectively. We apply a microstructure evolution model based on rate theory to estimate the dose-dependent concentration of oxygen vacancies in the defected lattice. The rate model predicts a saturation at low dose levels for irradiations at room temperature, while for irradiations at 600°C, the saturation limit for the population of oxygen vacancies occurs at a significantly higher dose. By utilizing the dose-dependent photoluminescence intensities in the irradiated thoria crystals, we obtain optimized migration barrier parameters for thorium and oxygen interstitials and oxygen vacancies that simultaneously capture the optical response of the crystals irradiated at room- and elevated-temperature. When combined with other characterization techniques, such as modulated thermoreflectance, XPS, XRD, TEM, and Raman spectroscopy, the proposed approach could provide new insight into defect formation, accumulation, and recombination on length-scales

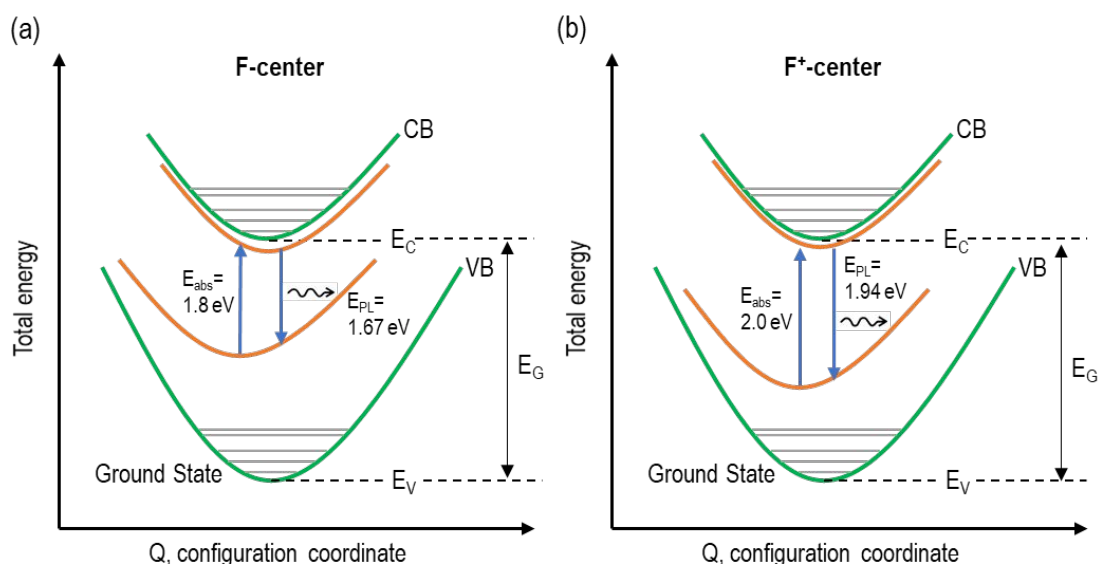


Figure 7. Schematic configuration coordinate diagram depicting possible electronic transitions due to (a) F- and (b) F⁺-center oxygen vacancy defects in the irradiated thoria crystals resulting in the observed optical absorption and photoluminescence phenomena. (VB: valence band, CB: conduction band, E_{abs} : optical absorption energy, E_{PL} : photoluminescence energy).

ranging from the single atomic level to extended defects on the order of several nanometers. This could also enable a fundamental understanding on the thermal transport mechanisms and other phenomena that contribute to a degradation of performance of energy materials in extreme environments.

Conflicts of interest

There are no conflicts to declare.

Acknowledgements

This work was supported by the Center for Thermal Energy Transport under Irradiation (TETI), an Energy Frontier Research Center funded by the US Department of Energy, Office of Science, Office of Basic Energy Sciences. This work utilized high performance computing resources provided by the Ohio Supercomputing Center. The authors would like to thank Lin Shao and Aaron French at Texas A&M University for providing ion irradiation support as part of a Nuclear Science User Facilities (NSUF) experiment funded through the US Department of Energy, Office of Nuclear Energy under DOE Idaho Operations Office Contract DE-AC07-05ID14517.

Notes and references

1. J. L. G. Fierro. *Metal oxides: chemistry and applications*: CRC press; 2005.
2. G. Korotcenkov. *Metal oxides in energy technologies*: Elsevier; 2018.
3. D. Nunes, A. Pimentel, L. Santos, P. Barquinha, L. Pereira, E. Fortunato, et al. *Metal oxide nanostructures: synthesis, properties and applications*: Elsevier; 2018.
4. Y. Zhu, Q. Lin, Y. Zhong, H. A. Tahini, Z. Shao, H. Wang. *Energy & Environmental Science*. 2020;**13**(10):3361-92.
5. G. Choppin, J.-O. Liljenzin, J. Rydberg. *Radiochemistry and nuclear chemistry*: Butterworth-Heinemann; 2002.
6. T. Montini, M. Melchionna, M. Monai, P. Fornasiero. *Chemical reviews*. 2016;**116**(10):5987-6041.
7. P. Arunkumar, M. Meena, K. S. Babu. *Nanomaterials and Energy*. 2012;**1**(5):288-305.
8. R. Devanathan. *Nuclear Instruments and Methods in Physics Research Section B: Beam Interactions with Materials and Atoms*. 2009;**267**(18):3017-21.
9. M. Khafizov, V. Chauhan, Y. Wang, F. Riyad, N. Hang, D. Hurley. *Journal of Materials Research*. 2017;**32**(1):204-16.
10. X.-Y. Liu, M. W. D. Cooper, K. J. McClellan, J. C. Lashley, D. D. Byler, B. Bell, et al. *Physical Review Applied*. 2016;**6**(4):044015.
11. J. White, A. Nelson. *Journal of nuclear materials*. 2013;**443**(1-3):342-50.
12. D. Laux, D. Baron, G. Despau, A. Kellerbauer, M. Kinoshita. *Journal of Nuclear Materials*. 2012;**420**(1-3):94-100.
13. S. Dutta, S. Chattopadhyay, A. Sarkar, M. Chakrabarti, D. Sanyal, D. Jana. *Progress in Materials Science*. 2009;**54**(1):89-136.
14. E. Kotomin, A. Popov. *Nuclear Instruments and Methods in Physics Research Section B: Beam Interactions with Materials and Atoms*. 1998;**141**(1-4):1-15.
15. D. Smith, D. Dexter. *V Optical Absorption Strengths of Defects in Insulators: The f-Sum Rule, Smakula's Equation, Effective Fields, and Application to Color Centers in Alkali Halides*. *Progress in Optics*. 10: Elsevier; 1972. p. 165-228.
16. K. Bawane, X. Liu, T. Yao, M. Khafizov, A. French, J. M. Mann, et al. *Journal of Nuclear Materials*. 2021;**552**:152998.
17. C. A. Dennett, Z. Hua, A. Khanolkar, T. Yao, P. K. Morgan, T. A. Prusnick, et al. *APL Materials*. 2020;**8**(11):111103.
18. M. Khafizov, J. Pakarinen, L. He, D. H. Hurley. *Journal of the American Ceramic Society*. 2019;**102**(12):7533-42.
19. C. Onofri, M. Legros, J. L chelle, H. Palancher, C. Baumier, C. Bachelet, et al. *Journal of Nuclear Materials*. 2017;**494**:252-9.
20. D. Yun, A. J. Oaks, W.-y. Chen, M. A. Kirk, J. Rest, Z. Z. Insopov, et al. *Journal of nuclear materials*. 2011;**418**(1-3):80-6.
21. J. M. Johnson, S. Im, W. Windl, J. Hwang. *Ultramicroscopy*. 2017;**172**:17-29.
22. B. Henderson, J. E. Wertz. 1977.
23. A. Smakula. *Zeitschrift f r Physik*. 1930;**59**(9):603-14.
24. E. Mollwo, W. Roos. *Math-Physik Kl*. 1934;**59**(8):107.
25. M. Gaft, R. Reisfeld, G. Panczer. *Modern luminescence spectroscopy of minerals and materials*: Springer; 2015.
26. A. d. S. Marfunin. *Spectroscopy, luminescence and radiation centers in minerals*: Springer Science & Business Media; 2012.
27. Y. Chen, J. Kolopus, W. Sibley. *Physical Review*. 1969;**186**(3):865.
28. P. Edel, Y. d'Aubigne, R. Romestain, B. Henderson, L. Kappers. *Journal of Physics C: Solid State Physics*. 1979;**12**(23):5245.
29. L. A. Kappers, R. L. Kroes, E. B. Hensley. *Physical Review B*. 1970;**1**(10):4151.
30. R. Krause-Rehberg, H. S. Leipner. *Positron annihilation in semiconductors: defect studies*1999.
31. N. Djourellov, B. Marchand, H. Marinov, N. Moncoffre, Y. Pipon, N. B ererd, et al. *Journal of nuclear materials*. 2013;**443**(1-3):562-9.
32. J. Ji, A. Colosimo, W. Anwand, L. Boatner, A. Wagner, P. Stepanov, et al. *Scientific reports*. 2016;**6**(1):1-9.
33. J. Wiktor, G. Jomard, M. Torrent, M. Bertolus. *Journal of Physics: Condensed Matter*. 2016;**29**(3):035503.
34. T. Yang, C. A. Taylor, C. Wang, Y. Zhang, W. J. Weber, J. Xiao, et al. *Journal of the American Ceramic Society*. 2015;**98**(4):1314-22.
35. A. Zubiaga, F. Plazaola, J. Garcia, F. Tuomisto, V. Mu oz-Sanjos , R. Tena-Zaera. *Physical Review B*. 2007;**76**(8):085202.
36. J. Perri re. *Vacuum*. 1987;**37**(5-6):429-32.
37. G. Gutierrez, C. Onofri, S. Miro, M. Bricout, F. Lepr tre. *Nuclear Instruments and Methods in Physics Research Section B: Beam Interactions with Materials and Atoms*. 2018;**434**:45-50.
38. T. Kaida, K. Kamioka, T. Ida, K. Kuriyama, K. Kushida, A. Kinomura. *Nuclear Instruments and Methods in Physics Research Section B: Beam Interactions with Materials and Atoms*. 2014;**332**:15-8.
39. C. Binet, A. Badri, J.-C. Lavalley. *The Journal of Physical Chemistry*. 1994;**98**(25):6392-8.
40. P. Patsalas, S. Logothetidis, C. Metaxa. *Applied Physics Letters*. 2002;**81**(3):466-8.
41. K. Winer, F. Wooten, C. Colmenares, R. Smith. *Journal of luminescence*. 1986;**35**(6):311-9.
42. M. Mann, D. Thompson, K. Serivalsatit, T. M. Tritt, J. Ballato, J. Kolis. *Crystal growth & design*. 2010;**10**(5):2146-51.
43. J. Bodine, F. Thiess. *Journal of the Franklin Institute*. 1955;**259**(6):550.
44. O. Weinreich, W. Danforth. *Physical Review*. 1952;**88**(4):953.
45. V. Neeley, J. Gruber, W. Gray. *Physical Review*. 1967;**158**(3):809.
46. B. Childs, P. Harvey, J. Hallett. *Journal of the American Ceramic Society*. 1970;**53**(8):431-5.

47. B. Childs, P. Harvey, J. Hallett. *Journal of the American Ceramic Society*. 1972;**55**(11):544-7.
48. P. Harvey, J. Hallett. *Journal of the Electrochemical Society*. 1976;**123**(3):398.
49. P. Harvey, J. Hallett. *Journal of Solid State Chemistry*. 1975;**12**(3-4):219-24.
50. E. T. Rodine, P. L. Land. *Physical Review B*. 1971;**4**(8):2701.
51. T. R. Griffiths, J. Dixon. *Journal of the Chemical Society, Faraday Transactions*. 1992;**88**(8):1149-60.
52. R. Mohun, L. Desgranges, J. L chelle, P. Simon, G. Guimbreti re, A. Canizar s, et al. *Nuclear Instruments and Methods in Physics Research Section B: Beam Interactions with Materials and Atoms*. 2016;**374**:67-70.
53. M. S. Bryan, L. Fu, K. Rickert, D. Turner, T. A. Prusnick, J. M. Mann, et al. *Communications Physics*. 2020;**3**(1):1-7.
54. C. A. Dennett, W. R. Deskins, M. Khafizov, Z. Hua, A. Khanolkar, K. Bawane, et al. *Acta Materialia*. 2021;**213**:116934.
55. W. J. Weber, Y. Zhang. *Current Opinion in Solid State and Materials Science*. 2019;**23**(4):100757.
56. J. F. Ziegler, M. D. Ziegler, J. P. Biersack. *Nuclear Instruments and Methods in Physics Research Section B: Beam Interactions with Materials and Atoms*. 2010;**268**(11-12):1818-23.
57. K. O. Egbo, C. P. Liu, C. E. Ekuma, K. M. Yu. *Journal of Applied Physics*. 2020;**128**(13):135705.
58. G. Bader, P. Ashrit, V.-V. Truong. *Applied optics*. 1998;**37**(7):1146-51.
59. J. Carrasco, C. Sousa, F. Illas, P. V. Sushko, A. L. Shluger. *The Journal of chemical physics*. 2006;**125**(7):074710.
60. F. Karsai, P. Tiwald, R. Laskowski, F. Tran, D. Koller, S. Gr fe, et al. *Physical Review B*. 2014;**89**(12):125429.
61. Y. Ma, M. Rohlfing. *Physical Review B*. 2008;**77**(11):115118.
62. J. P. Perdew, A. Zunger. *Physical Review B*. 1981;**23**(10):5048.
63. P. Giannozzi, S. Baroni, N. Bonini, M. Calandra, R. Car, C. Cavazzoni, et al. *Journal of physics: Condensed matter*. 2009;**21**(39):395502.
64. R. I. Palomares, C. L. Tracy, F. Zhang, C. Park, D. Popov, C. Trautmann, et al. *Journal of Applied Crystallography*. 2015;**48**(3):711-7.
65. C. Matthews, R. Perriot, M. W. Cooper, C. R. Stanek, D. A. Andersson. *Journal of Nuclear Materials*. 2019;**527**:151787.
66. R. Stoller. *Comprehensive nuclear materials*. 2012:293-332.
67. V. S. Chauhan, J. Pakarinen, T. Yao, L. He, D. H. Hurley, M. Khafizov. *Materialia*. 2021;**15**:101019.
68. L. He, M. Khafizov, C. Jiang, B. Tyburska-P schel, B. J. Jaques, P. Xiu, et al. *Acta Materialia*. 2021;**208**:116778.
69. H. Fujiwara. *Spectroscopic ellipsometry: principles and applications*: John Wiley & Sons; 2007.
70. A. Mock, C. Dugan, S. Knight, R. Korlacki, J. M. Mann, M. M. Kimani, et al. *Applied Physics Letters*. 2019;**114**(21):211901.
71. J. Price, P. Lysaght, S. Song, H.-J. Li, A. Diebold. *Applied Physics Letters*. 2007;**91**(6):061925.
72. C. Sevik, T.  ađın. *Physical Review B*. 2009;**80**(1):014108.
73. A. Khanolkar, C. A. Dennett, Z. Hua, J. M. Mann, D. H. Hurley, M. Khafizov. 2021.
74. H. Y. Xiao, W. J. Weber. *The Journal of Physical Chemistry B*. 2011;**115**(20):6524-33.
75. P. Rinke, A. Schleife, E. Kioupakis, A. Janotti, C. R dl, F. Bechstedt, et al. *Physical review letters*. 2012;**108**(12):126404.
76. A. Koshkinbayeva, A. Abdullaev, Z. Nurekeyev, V. Skuratov, Y. Wang, M. Khafizov, et al. *Nuclear Instruments and Methods in Physics Research Section B: Beam Interactions with Materials and Atoms*. 2020;**475**:14-9.
77. K. Schwartz, C. Trautmann, A. El-Said, R. Neumann, M. Toulemonde, W. Knolle. *Physical Review B*. 2004;**70**(18):184104.
78. B. D. Evans. *Journal of nuclear materials*. 1995;**219**:202-23.
79. F. Leiter, H. Alves, D. Pfisterer, N. Romanov, D. Hofmann, B. Meyer. *Physica B: Condensed Matter*. 2003;**340**:201-4.
80. P. Tiwald, F. Karsai, R. Laskowski, S. Gr fe, P. Blaha, J. Burgd rfer, et al. *Physical Review B*. 2015;**92**(14):144107.
81. A. Mang, K. Reimann. *Solid state communications*. 1995;**94**(4):251-4.
82. K. W. B er, U. W. Pohl. *Optical Properties of Defects. Semiconductor Physics*: Springer, Cham; 2018.
83. C. Onofri, C. Sabathier, H. Palancher, G. Carlot, S. Miro, Y. Serruys, et al. *Nuclear Instruments and Methods in Physics Research Section B: Beam Interactions with Materials and Atoms*. 2016;**374**:51-7.
84. M. Kumar, V. K. Tripathi, R. Nagarajan. *Ceramics International*. 2019;**45**(9):11709-16.
85. A. Miskowiec, J. L. Niedziela, T. L. Spano, M. W. Ambrogio, S. Finkeldei, R. Hunt, et al. *Journal of Nuclear Materials*. 2019;**527**:151790.
86. A. Debelle, J.-P. Crocombette, A. Boule, A. Chartier, T. Jourdan, S. Pellegrino, et al. *Physical Review Materials*. 2018;**2**(1):013604.
87. M. Khafizov, M. F. Riyad, Y. Wang, J. Pakarinen, L. He, T. Yao, et al. *Acta Materialia*. 2020;**193**:61-70.
88. M. Bazzan, C. Sada. *Applied Physics Reviews*. 2015;**2**(4):040603.
89. H. Chen, M. Buric, P. R. Ohodnicki, J. Nakano, B. Liu, B. T. Chorpene. *Applied Physics Reviews*. 2018;**5**(1):011102.
90. K. McCary, B. Wilson, J. Daw, P. Calderoni, C. M. Petrie, T. E. Blue. In-pile OFDR sensing with fiber Bragg gratings in sapphire optical fiber. Oak Ridge National Lab.(ORNL), Oak Ridge, TN (United States); 2019.